#### **ORIGINAL PAPER**





# Role of perovskite thickness on optoelectronic properties in lead bromide and lead iodide thin film perovskites: A DFT study

David R. Graupner Dmitri Kilin David R. Graupner

Received: 29 March 2023 / Accepted: 5 September 2023 / Published online: 13 September 2023 © The Author(s), under exclusive licence to The Materials Research Society 2023

#### Abstract

Two-dimensional organic—inorganic hybrid lead halide perovskites are of interest for photovoltaic and light emitting devices due to their favorable properties that can be tuned. Here we use density functional theory to model two-dimensional lead halide perovskites of different thicknesses and using two different hallogens. Excited-state optoelectronic properties of the perovskite models are examined using excited-state dynamics treated by reduced density matrix method. Nonadiabatic couplings were computed based on the on-the-fly approach along a molecular dynamics trajectory at ambient temperatures. The density matrix-based equation of motion for electronic degrees of freedom was used to determine the dynamics of electronic degrees of freedom. We observe that the thickness of the perovskite layer shows a redshift in the absorption spectra with increasing thickness but has minimal effect on the photoluminescence quantum yield of the material.

### Introduction

A popular candidate for next generation optoelectronic devices are thin film  $CsPbX_3$  (X = Cl, Br, I) lead halide perovskites (LHPs) due to their increased stability when compared to the bulk LHPs [1] and favorable optoelectronic properties [2–5]. The stability of the two-dimensional (2D) perovskites is dictated by their confinement regime [6]. Variation of layer thickness, while yet being away from the threedimensional (3D) bulk regime is expected to have qualitatively similar degree of stability. Thin film perovskites structures possess natural quantum-well structures due to the insulating qualities of the organic molecules in the structure [7]. These quantum wells induce both dielectric and quantum confinement effects [8], with the strong confinements leading to large exciton binding energies [9]. 2D LHPs are categorized by the relative stacking of the perovskite layers with Ruddlesden-Popper (RP) phase [10] and Dion-Jacobson (DJ) phase [11, 12] being the most common structures for < 100 >. The DJ perovskites exhibit an offset of (0, 0)between perovskite layers due to the divalent organic spacers, while the RP perovskites show an offset of (1/2, 1/2).

The formula for thin film LHPs is  $A_{n'}A_{n-1}M_nX_{3n+1}$ (A' = monovalent or divalent organic cation; n' = 2 or 1; A = Cs<sup>+</sup>, methylammonium (MA), formadamidinium (FA);  $M = Pb^{2+}$ ,  $Sn^{2+}$ , etc.;  $X = Cl^{-}$ ,  $Br^{-}$ ,  $I^{-}$ ). Thin film LHPs are classified based on the thickness of the inorganic layer as indicated in the formula by n (n = 1, 2, 3, etc.) [13]. Adjusting the thickness of the thin film LHPs can be used to tune the emission properties of the material. Further, it is observed that thin film perovskites often form in a structures with varying thicknesses rather than a structure with a single thickness due to the similar formation energies of the different thickness thin film perovskites [14]. The mix of different thickness thin film perovskites results in heterostructures that offer the possibilities of manipulation of the recombination, transport, and generation of charge carriers due to the change in band gap energies at the heterojunction [15].

Here we report the effects that changing the thickness of the inorganic layer of the thin film LHPs provides for the photoluminescence (PL) of the materials. The models examined in this paper are DJ perovskites with n = 1, 2, 3, or 4, Cs<sup>+</sup> for A, butyl diammonium (BdA) molecules as A', and Br<sup>-</sup> or I<sup>-</sup> for X. Figure 1 and Figure S1 show the lead iodide and lead bromide models, respectively. Increasing the thickness of the inorganic layer is expected to cause a redshift in the emission and absorption of the material, while changing the halide from bromide to iodide is expected to give a further redshift. Excited-state dynamics



<sup>☐</sup> Dmitri Kilin dmitri.kilin@ndsu.edu

Department of Chemistry and Biochemistry, North Dakota State University, Fargo, ND 58108, USA

902 D. R. Graupner, D. Kilin

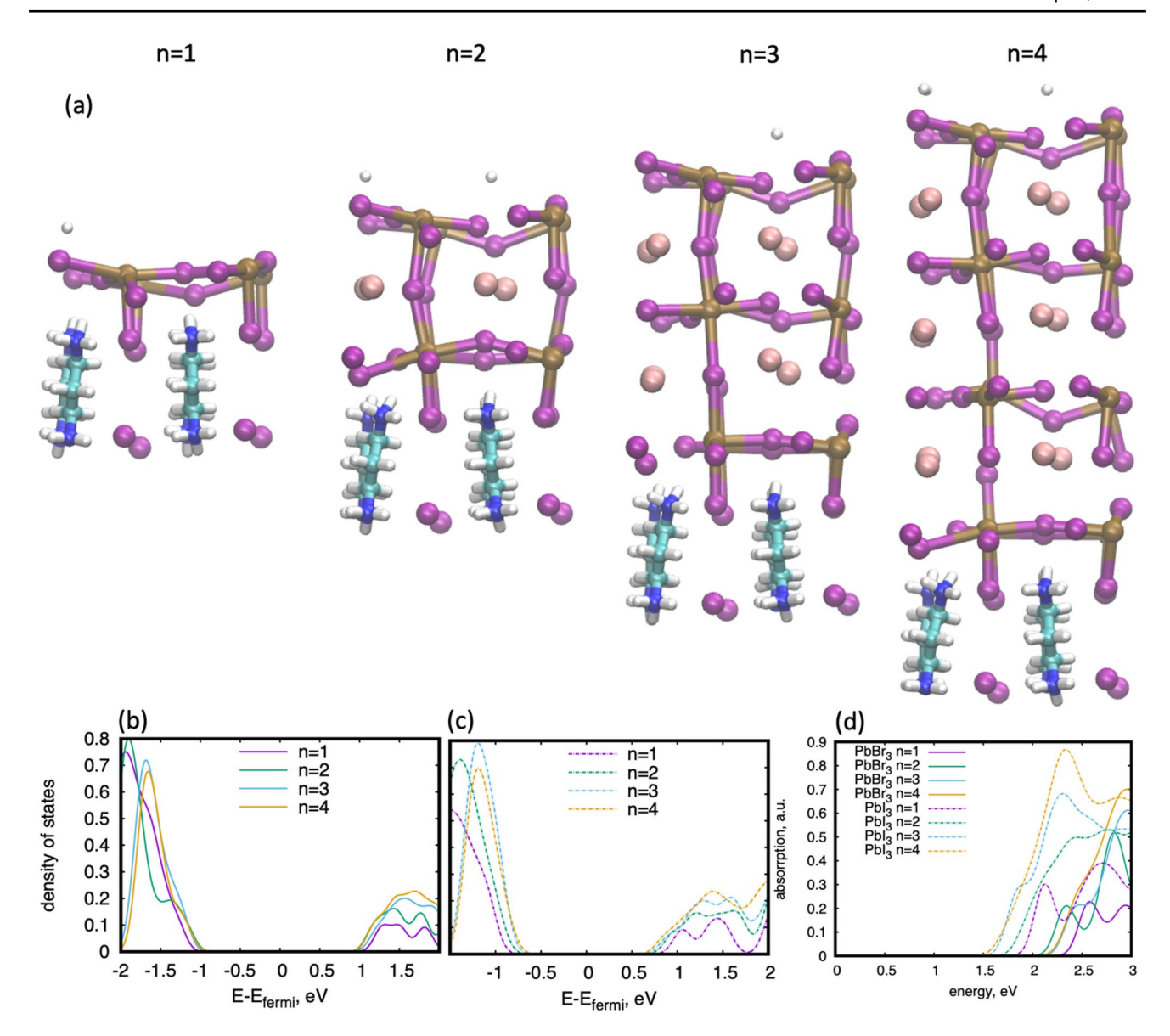


**Fig. 1 a** Atomistic models of lead iodide organic–inorganic hybrid perovskite with n = 1, 2, 3, and 4. White, cyan, blue, brown, purple, and pink spheres represent hydrogen, carbon, nitrogen, lead, iodine, and cesium atoms, respectively. Atomistic models of lead bromide hybrid perovskite can be seen in Figure S1. Density of states for **b** lead bromide (solid) and **c** lead iodide (dot-dash) hybrid perovskites

with n=1 (purple), n=2 (green), n=3 (blue), and n=4 (orange). Choice of which states to focus on for the n=3 and n=4 models is responsible for the decrease in the density of states in the region below -1.5 eV. **d** Computed absorptions spectra for lead bromide and lead iodide hybrid perovskites

and are used to characterize the PL properties and are calculated from the computed nonadiabatic couplings (NACs) between nuclear and electronic degrees of freedom from adiabatic molecular dynamics trajectories. The reduced density matrix formalism within Redfield theory is used to compute nonradiative relaxation rates from the NACs [16, 17]. Nonradiative and radiative recombination rates, computed from Einstein coefficients, are then used to calculate the PL quantum yield (PLQY) [18].

#### Methods

## **Computational details**

The ground state electronic structure was calculated using density functional theory (DFT) with the generalized gradient approximation (GGA) Perdew-Burke-Ernzerhof (PBE) functional [19] in a plane-wave basis set along with projector augmented-wave (PAW) pseudopotentials [20, 21] in Vienna Ab initio Simulation Package



(VASP) [22]. Subsequent single point calculations were performed using noncollinear spin DFT including the spin—orbit coupling (SOC) interaction and used to compute observables for the systems. The model has a structure of  $BdA_4Cs_{4(n-1)}Pb_{4n}X_{12n+4}$ , where X is either Br or I. All calculations were performed at the  $\Gamma$  point.

## **Theory**

Details of the electronic basis and computed observables are provided in the supplemental information (SI).

#### **Results and discussion**

Figure 1 panels (b, c) show the ground state density of states (DOS) for the lead Bromide and lead iodide models, respectively, and (d) shows the computed absorption spectra. The shape of the DOS and absorptions show good qualitative agreement between the different thicknesses and halides. The redshift of the absorption and band gap energy for the lead iodide models when compared to the lead bromide models is expected. Increasing the thickness of the layers redshifts the initial absorption spectra in agreement with the expectations of quantum confinement, with the exception of the n=3 and n=4 lead bromide models. This is attributed to geometry distortions for these models which can lead to charge transfer states leading to a reduced oscillator strength

for these transitions. The total energy of the models and its relationship to the number of atoms, number of electrons, and volume of the simulation cell is shown in Table S1. We see that for both halides that the total energy increases with increasing perovskite thickness when considering the number of atoms, number of electrons, or volume of simulation cell, with the lead bromide models showing a lower energy than the lead iodide models of the same thickness. The spinor Kohn–Sham orbitals (SKSO) for the frontier orbitals, Figure S2 and S3, show a spatial separation between the highest occupied and lowest unoccupied SKSO into different regions of the perovskite layer for the n=3 and n=4 lead bromide models. For each of other models occupied and unoccupied frontier orbitals share the same spatial localization.

The Redfield tensors, illustrated in Figure S4, represent the rates of state-to-state transitions in units of ps<sup>-1</sup> and are used to calculate the nonradiative dissipation. Figure 2 shows trajectories of nonradiative dissipation from the initial nonequilibrium excited-state to the lowest excited-state. The initial excited-state is chosen to be the *interband* transition with the largest oscillator strength that does not include one of the frontier orbitals or their near-degenerate states. The SKSOs for the initial conditions are shown in Figure S2 and S3. A mismatch between the frequency of available normal modes and electronic transition energy is resulting in long lived excited-states. This causes the relaxation lifetime for the hole  $(\tau_h)$  and electron  $(\tau_e)$  to appear later in the figure

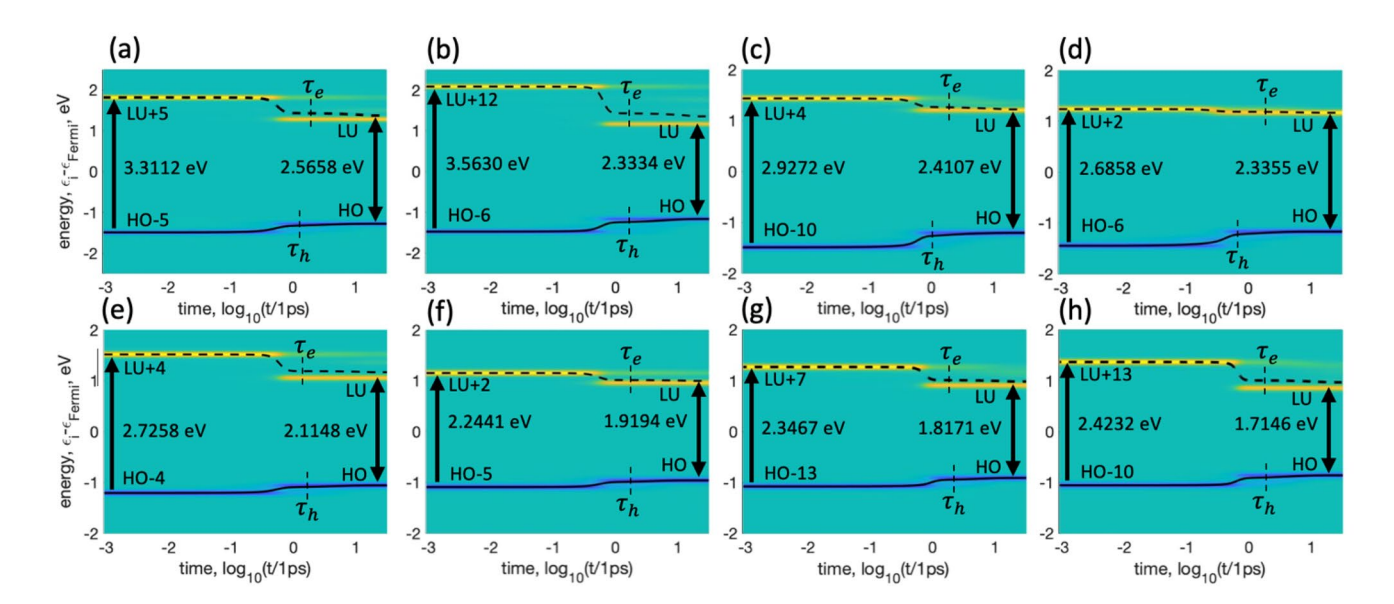


**Fig. 2** Nonradiative relaxation for the  $(\mathbf{a}-\mathbf{d})$  lead bromide models and  $(\mathbf{e}-\mathbf{h})$  lead iodide models with  $(\mathbf{a}, \mathbf{e})$  n=1,  $(\mathbf{b}, \mathbf{f})$  n=2,  $(\mathbf{c}, \mathbf{g})$  n=3, and  $(\mathbf{d}, \mathbf{h})$  n=4. The green color indicates background reference charge density. The yellow line represents the charge density of the electron, while the blue line represents the charge density of the hole. The vertical dashed lines labeled with  $\tau_h$  and  $\tau_e$  represent time of

relaxation from HO-x and LU+y, respectively. The energy expectation value for the hole and electron is represented by the horizontal solid and dashed lines, respectively. The initial conditions for all models represent the highest oscillator strength excitation that does not involve one of the near-degenerate principal band gap orbitals



than the energy expectation values appear to indicate. Figure S5 examines the relationship between  $\tau_h$  and  $\tau_e$  and the excitation energy for the hole and electron, respectively. The lifetimes are qualitatively group together and follow the general trend of increased lifetime for larger initial excitation, according to gap law. The n=4 lead bromide model is an outlier from this trend for the hole relaxation, where it exhibits a shorter lifetime than the other models. While for the electron relaxation, the n=3 and n=4 lead bromide models appear as outliers with both exhibiting longer lifetimes and a decrease in lifetime for larger excitations.

Radiative recombination, resulting in the emitted photons, is a mechanism competing with nonradiative dissipation, resulted in emitted phonons. Figure 3 shows the timeresolved emission, Eq. S21 and time-integrated emission, Eq. S22, for the models monitored along the excited-state trajectory. The initial conditions are the same as those for Fig. 2. The initial earlier emission event is at the initial excitation energy and occurs before cooling to the band gap. Emissions from the HO-LU transitions occur once the hot-carriers cool to the lowest excitation at the bandgap. Next, one compares intensities of the emission peaks of the interband (e.g., LU  $\rightarrow$  HO) and intraband (e.g., LU + 2  $\rightarrow$ LU) nature. It is observed that the emission at the LU  $\rightarrow$ HO transition is the most intense for all the models among all interband transitions. The intensity of the interband LU → HO transition is comparable to the intensities of *intra*band transitions for all models except the n=3 and n=4lead bromide and n=1 lead iodide models. These specific

models show approximately two orders of magnitude greater intensity for the LU  $\rightarrow$  HO *interband* transition than any of the *intraband* transitions. A hypothetic explanation of this feature is based on specific confinement regime that tunes the electronic subgaps to vibrational frequencies in these models, yielding the quickest cascading down to the lowest excitation, which decreases the *intraband* transitions at larger time values. This decreases the time-integrated PL intensity for these *intraband* transitions.

We compute PLQY, Eq. S24, to determine the efficiency of PL using radiative relaxation rate  $(k_r)$  and nonradiative relaxation rate  $(k_{nr})$ . The Redfield tensor element  $R_{HO-LU}$  is used for  $k_{nr}$ , Eq. S16 and the Einstein coefficient for spontaneous emission in terms of oscillator strength is used to

**Table 1** Oscillator strength  $f_{ij}$ , radiative recombination rate  $k_r$ , nonradiative recombination rate  $k_{nr}$ , Resultant PLQYs for each model studied

Model	$f_{\rm ij}$	k <sub>r</sub> [1/fs]	k <sub>nr</sub> [1/fs]	PLQY
Lead bromide $n=1$	0.83	$1.70 \times 10^{-6}$	$2.43 \times 10^{-6}$	0.3514
Lead bromide $n=2$	0.79	$1.77 \times 10^{-6}$	$1.65 \times 10^{-6}$	0.4671
Lead bromide $n=3$	0.70	$1.32 \times 10^{-6}$	$3.68 \times 10^{-7}$	0.5041
Lead bromide $n=4$	0.22	$2.76 \times 10^{-7}$	$7.97 \times 10^{-7}$	0.2211
Lead iodide $n = 1$	1.82	$1.76 \times 10^{-6}$	$6.87 \times 10^{-7}$	0.5995
Lead iodide	0.39	$4.69 \times 10^{-7}$	$5.40 \times 10^{-7}$	0.4220
n=2				
Lead iodide $n=3$	1.08	$8.60 \times 10^{-7}$	$2.46 \times 10^{-7}$	0.6657
Lead iodide $n=4$	0.17	$2.84 \times 10^{-7}$	$8.34 \times 10^{-8}$	0.7707

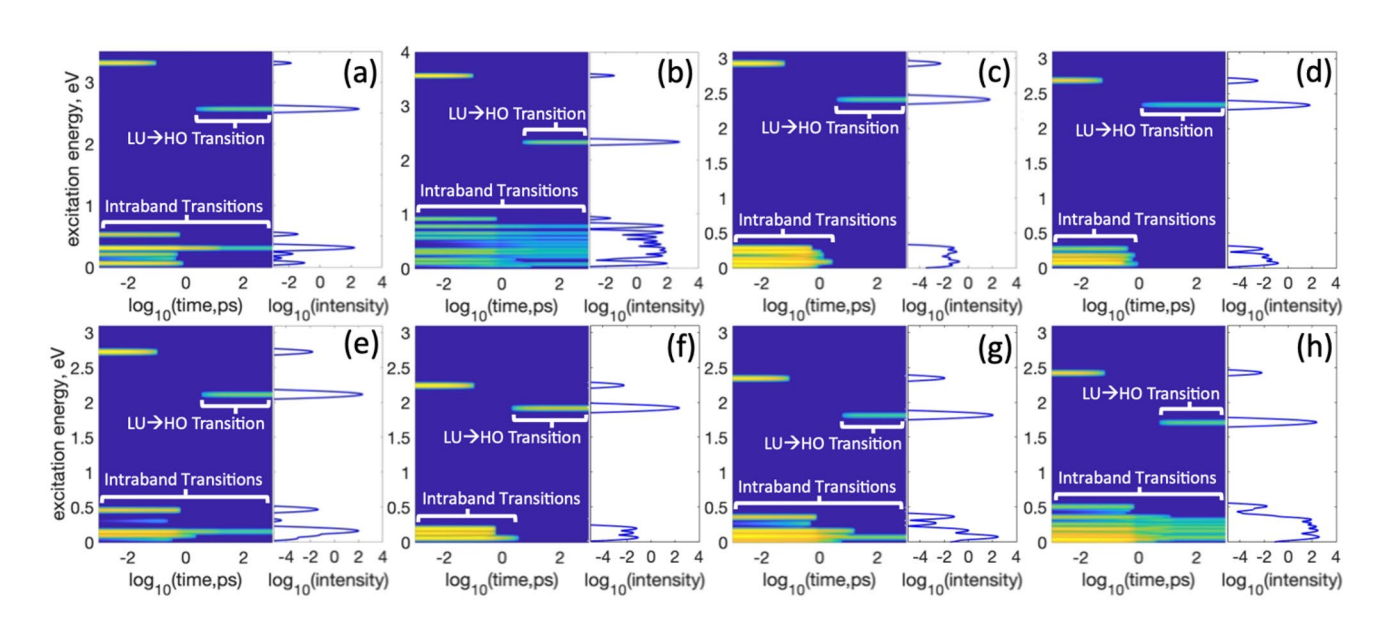


**Fig. 3** Radiative relaxation along the excited-state electronic dynamics trajectory for the  $(\mathbf{a}-\mathbf{d})$  lead bromide models and  $(\mathbf{e}-\mathbf{h})$  lead iodide models with  $(\mathbf{a}, \mathbf{e})$  n=1,  $(\mathbf{b}, \mathbf{f})$  n=2,  $(\mathbf{c}, \mathbf{g})$  n=3, and  $(\mathbf{d}, \mathbf{h})$  n=4. The left graph in each panel shows the time-resolved PL, while the right graph shows the time-integrated PL. The initial conditions for

this figure correspond to those in Fig. 2. The blue background corresponds to no PL at a given time and transition energy. Natural colors from blue to yellow correspond to increasing intensity of the time-resolved PL. For each model, it is observed that the LU  $\rightarrow$  HO transition is the most intense non-intraband transition



calculate  $k_r$ , Eq. S23. Table 1 shows the  $k_r$ ,  $k_{nr}$ , and PLQY for the lead bromide and lead iodide models. The oscillator strength shown here is for the LU → HO transition but the radiative and nonradiative rates of relaxation and PLQY shown factor in all four transitions between the near-degenerate LU and HO states. The values for the each unique neardegenerate transition can be seen in Table S2. The effect that thickness of the perovskite layer and halide identity shows on the PLQY is largely due to the decreasing values of the Redfield tensor elements with size and when bromide is replaced with iodide. The oscillator strength values do not vary based on the thickness of the perovskite or halogen used except for the n=4 lead bromide model, which has lower oscillator strength values due to the distorted geometry of the model. This results in the k, to vary with minimal influence on the specific model studied.

#### **Conclusion**

Here we use density functional theory and nonadiabatic excited-state dynamics calculations to explore the photophysical properties of two-dimensional hybrid lead halide perovskites. We observed a decrease in intensity of intraband photoluminescence for lead halide perovskites that show an increased population in excited-states for longer periods of time. This effect appears to be unaffected by the thickness of the perovskite layer or the halogen studied. The observed increase of the PLQY is an interesting feature that may provide benefits for the applications. The effort of this work was focused on identifying trends and rational reasons for the trends. A control over such features of this class of material as bandgap and PLQY by tuning layer thickness is an important fundamental knowledge. Knowledge of the trends can be used for applications: it is not necessarily needed that increase or decrease of thickness give specific influence over the observables—it is more important to have a record of correlation between size and PLQY that can be used for applications. The PLQY varies in relation to the relative values of oscillator strength, which do not appear to be dependent on thickness of perovskite or halogen studied, and the Redfield tensor elements. This causes the PLQY to have only a minimal dependence on the thickness of the model. It is observed that the values of the band gap and first absorption peak do vary with the thickness of the perovskite layer, with thicker layers showing redshifted energy, and with the choice of halogen used in the model, with the larger iodide being more redshifted than the bromide. Additionally, we observe that the lead iodide models act as intuitively expected, but the lead bromide models challenge the intuitive expectations. Further calculations are needed to determine if the geometry distortions are an intrinsic feature of the lead bromide perovskite materials.

Supplementary Information The online version contains supplementary material available at https://doi.org/10.1557/s43580-023-00641-y.

Acknowledgments D.R.G. Thanks NSF CHE-2004197 for support. D.K. acknowledges the support of the National Science Foundation under Grant CHE-1944921. Authors thank the DOE BES NERSC facility for computational resources, allocation award "Computational Modeling of Photo-catalysis and Photo-induced Charge Transfer Dynamics on Surfaces", supported by the Office of Science of the DOE under Contract DE-AC02-05CH11231. Authors also thank Aaron Forde, Yulun Han, Landon Johnson, and Steven Westra for collective discussion and editing. D.K. thanks David Micha, Oleg Prezhdo, Sergei Tretiak, Svetlana Kilina, Andrei Kryjevski for inspiring discussions.

**Funding** The funding was provided by Directorate for Mathematical and Physical Sciences, (1944921, 2004197).

**Data availability** The data that supports the above-presented results are available from the corresponding author upon reasonable request.

#### **Declarations**

**Conflict of interest** The authors report there are no competing interests to declare.

#### References

- F. Arabpour Roghabadi, M. Alidaei, S.M. Mousavi, T. Ashjari, A.S. Tehrani, V. Ahmadi, S.M. Sadrameli, J. Mater. Chem. A 7, 5898–5933 (2019). https://doi.org/10.1039/C8TA10444A
- L. Protesescu, S. Yakunin, M.I. Bodnarchuk, F. Krieg, R. Caputo, C.H. Hendon, R.X. Yang, A. Walsh, M.V. Kovalenko, Nano Lett. 15, 3692–3696 (2015), https://doi.org/10.1021/nl5048779
- T.M. Koh, V. Shanmugam, J. Schlipf, L. Oesinghaus, P. Muller-Buschbaum, N. Ramakrishnan, V. Swamy, N. Mathews, P.P. Boix, S.G. Mhaisalkar, Adv. Mater. 28, 3653–3661 (2016). https://doi.org/10.1002/adma.201506141
- H. Dong, C. Ran, W. Gao, M. Li, Y. Xia, W. Huang, eLight 3, 3 (2023). https://doi.org/10.1186/s43593-022-00033-z
- M.P. Esch, Y. Shu, B.G. Levine, J. Phys. Chem. A 123, 2661–2673 (2019). https://doi.org/10.1021/acs.jpca.9b00952
- T.L. Leung, I. Ahmad, A.A. Syed, A.M.C. Ng, J. Popović, A.B. Djurišić, Commun. Mater. 3, 63 (2022). https://doi.org/10.1038/ s43246-022-00285-9
- D. Ghosh, A.J. Neukirch, S. Tretiak, J. Phys. Chem. Lett. 11, 2955–2964 (2020). https://doi.org/10.1021/acs.jpclett.0c00594
- K. Wang, J.Y. Park, R. Akriti, L. Dou, EcoMat 3, e12104 (2021). https://doi.org/10.1002/eom2.12104
- J.C. Blancon, A.V. Stier, H. Tsai, W. Nie, C.C. Stoumpos, B. Traoré, L. Pedesseau, M. Kepenekian, F. Katsutani, G.T. Noe, J. Kono, S. Tretiak, S.A. Crooker, C. Katan, M.G. Kanatzidis, J.J. Crochet, J. Even, A.D. Mohite, Nat. Commun. 9, 2254 (2018). https://doi.org/10.1038/s41467-018-04659-x
- C.C. Stoumpos, D.H. Cao, D.J. Clark, J. Young, J.M. Rondinelli, J.I. Jang, J.T. Hupp, M.G. Kanatzidis, Chem. Mater. 28, 2852– 2867 (2016). https://doi.org/10.1021/acs.chemmater.6b00847
- M. Dion, M. Ganne, M. Tournoux, Mater. Res. Bull. 16, 1429– 1435 (1981). https://doi.org/10.1016/0025-5408(81)90063-5
- A.J. Jacobson, J.W. Johnson, J.T. Lewandowski, Inorg. Chem. 24, 3727–3729 (1985). https://doi.org/10.1021/ic00217a006
- L. Mao, W. Ke, L. Pedesseau, Y. Wu, C. Katan, J. Even, M.R. Wasielewski, C.C. Stoumpos, M.G. Kanatzidis, J. Am. Chem.



906 D. R. Graupner, D. Kilin

Soc. 140, 3775–3783 (2018). https://doi.org/10.1021/jacs.8b00542

- L.N. Quan, M. Yuan, R. Comin, O. Voznyy, E.M. Beauregard, S. Hoogland, A. Buin, A.R. Kirmani, K. Zhao, A. Amassian, D.H. Kim, E.H. Sargent, J. Am. Chem. Soc. 138, 2649–2655 (2016). https://doi.org/10.1021/jacs.5b11740
- C.P. Clark, J.E. Mann, J.S. Bangsund, W.-J. Hsu, E.S. Aydil, R.J. Holmes, ACS Energy Lett. 5, 3443–3451 (2020). https://doi.org/ 10.1021/acsenergylett.0c01609
- D.R. Graupner, D.S. Kilin, J. Appl. Spectrosc. 90, 436–447 (2023). https://doi.org/10.1007/s10812-023-01551-5
- A. Forde, T. Inerbaev, E.K. Hobbie, D.S. Kilin, J. Am. Chem. Soc. 141, 4388–4397 (2019). https://doi.org/10.1021/jacs.8b13385
- D.R. Graupner, D.S. Kilin, MRS Adv. 7, 772–777 (2022). https://doi.org/10.1557/s43580-022-00358-4
- J.P. Perdew, K. Burke, M. Ernzerhof, Phys. Rev. Lett. 78, 1396– 1396 (1997). https://doi.org/10.1103/PhysRevLett.78.1396

- G. Kresse, D. Joubert, Phys. Rev. B 59, 1758–1775 (1999). https://doi.org/10.1103/PhysRevB.59.1758
- P.E. Blöchl, Phys. Rev. B 50, 17953–17979 (1994). https://doi. org/10.1103/PhysRevB.50.17953
- G. Kresse, J. Furthmüller, Comput. Mater. Sci. 6, 15–50 (1996). https://doi.org/10.1016/0927-0256(96)00008-0

**Publisher's Note** Springer Nature remains neutral with regard to jurisdictional claims in published maps and institutional affiliations.

Springer Nature or its licensor (e.g. a society or other partner) holds exclusive rights to this article under a publishing agreement with the author(s) or other rightsholder(s); author self-archiving of the accepted manuscript version of this article is solely governed by the terms of such publishing agreement and applicable law.